

LETTER TO THE EDITOR

Low power jet-ISM interaction in NGC 7319 revealed by JWST/MIRI MRS

M. Pereira-Santaella^{1,2}, J. Álvarez-Márquez¹, I. García-Bernete³, A. Labiano^{4,5}, L. Colina¹, A. Alonso-Herrero⁵,
E. Bellocchi^{6,7}, S. García-Burillo², S. F. Hönig⁸, C. Ramos Almeida^{9,10}, and D. Rosario¹¹

(Affiliations can be found after the references)

March 31, 2024

ABSTRACT

We present JWST/MIRI MRS spectroscopy of NGC 7319, the largest galaxy in the Stephan's Quintet, observed as part of the Early Release Observations (ERO). NGC 7319 hosts a type 2 active galactic nucleus (AGN) and a low-power radio jet ($L_{1.4\text{GHz}}=3.3\times10^{22}\text{ W Hz}^{-1}$) with two asymmetric radio hotspots at 430 pc (N2) and 1.5 kpc (S2) projected distances from the unresolved radio core. The MRS data suggest that the molecular material in the disk of the galaxy decelerates the jet and causes this length asymmetry. We find enhanced emission from warm and hot H_2 ($T_w=330\pm40\text{ K}$, $T_h=900\pm60\text{ K}$) and ionized gas at the intersection between the jet axis and dust lanes in the disk. This emission is coincident with the radio hotspot N2 closest to the core, suggesting that the jet-interstellar medium (ISM) interaction decelerates the jet. Conversely, the mid-infrared emission at the more distant hotspot is fainter, more highly ionized, and with lower H_2 excitation, suggesting a more diffuse atomic environment where the jet can progress to farther distances. At the N2 radio hotspot, the ionized gas mass ($M_{\text{ion}}=(2.4-12)\times10^5 M_\odot$) is comparable to that of the warm H_2 , but the former is more turbulent ($\sigma_{\text{ion}}\sim300$ vs. $\sigma_{\text{H}_2}\sim150\text{ km s}^{-1}$), so the mechanical energy of the ionized gas is $\sim1.3-10$ times higher. From these estimates, we find that only $<0.2\%$ of the jet energy remains as mechanical energy in these two ISM phases at N2. We also find extended ($r>0.3-1.5\text{ kpc}$) high-ionization emission ([Mg v], [Ne vi], and [Ne v]) close to the radio hotspots. This initial analysis of NGC 7319 shows the potential of MIRI/MRS to investigate the AGN feedback mechanisms due to radio jets and their radiation field in the, often heavily dust-enshrouded, central regions of galaxies. Understanding these mechanisms is an essential ingredient in the development of cosmological simulations of galaxy evolution.

Key words. galaxies: ISM – galaxies: jets – infrared: galaxies

1. Introduction

James Webb Space Telescope (JWST) observations of NGC 7319 were obtained as part of the Early Release Observations (ERO; Program ID #2732, PI K. M. Pontoppidan). In this Letter, we focus on the analysis of the Mid-Infrared Instrument (MIRI) medium resolution spectrograph (MRS) data (Rieke et al. 2015; Wells et al. 2015; Wright et al. 2015).

NGC 7319 is the largest galaxy in the Stephan's Quintet interacting group (Arp 319, HCG 092; $d = 98\text{ Mpc}$). NGC 7319 lost most of its atomic neutral gas during the interactions (Williams et al. 2002), but some atomic ionized and cold molecular gas is still present in its nuclear region (Rodríguez-Baras et al. 2014; Gao & Xu 2000). This galaxy hosts a type 2 active galactic nucleus (AGN), which dominates the energy output of this object since no strong nuclear starburst signatures are found (Sulentic et al. 2001). From X-ray spectral fitting in Ricci et al. (2017), the intrinsic hard X-ray (14–195 keV) luminosity of $10^{43.8}\text{ erg s}^{-1}$ places the AGN in the range of local Seyferts, while the high column density ($N_{\text{H}}=10^{23.8}\text{ cm}^{-2}$) is consistent with its obscured nature. Two asymmetric radio lobes and a compact core are detected suggesting the presence of a low-power radio jet with $L_{1.4\text{GHz}}=10^{22.5}\text{ W Hz}^{-1}$ (Aoki et al. 1999; Xanthopoulos et al. 2004).

Low-power radio jets produced by AGN seem to have an important role in galaxy evolution by providing kinetic feedback to the host interstellar medium (ISM) and regulating the formation of stars (e.g., Weinberger et al. 2017; Davé et al. 2019). The jet interaction with the cold molecular and ionized ISM phases has

been studied in a few local galaxies and AGN with low L_{AGN} and $L_{1.4\text{GHz}}$, similar to NGC 7319, using sub-mm and optical data (e.g., Alatalo et al. 2011; García-Burillo et al. 2014, 2019; Alonso-Herrero et al. 2018; Fernández-Ontiveros et al. 2020; García-Bernete et al. 2021; Venturi et al. 2021). Previous mid-IR spectroscopic studies, however, focused on more luminous radio galaxies (e.g., Ogle et al. 2010; Guillard et al. 2012; Dasyra et al. 2014; Zakamska et al. 2016) and were unable to provide spatially resolved information. In kinetic feedback studies, mid-IR emission lines are particularly valuable because they can trace from warm molecular gas ($\sim100-1000\text{ K}$) to highly ionized gas (coronal lines) and are less subject to extinction effects than optical/UV lines. In this Letter, we analyze the low-power jet-ISM interaction in NGC 7319 using MIRI/MRS data, which provides, for the first time, spatially resolved morphologies and kinematics.

2. Data reduction and analysis

2.1. JWST MIRI/MRS integral field spectroscopy

We processed the MIRI/MRS observations using the JWST calibration pipeline to produce the twelve spectral cubes with the default spatial and spectral sampling. Technical details on the data reduction are described in Appendix A.1.

We obtained maps of the brightest emission lines in this spectral range (Table B.1) by subtracting the local continuum (estimated with a linear fit) and integrating the line flux spaxel by spaxel between $\pm1100\text{ km s}^{-1}$, which is the velocity range where emission is detected for the broader ionized gas lines. We also

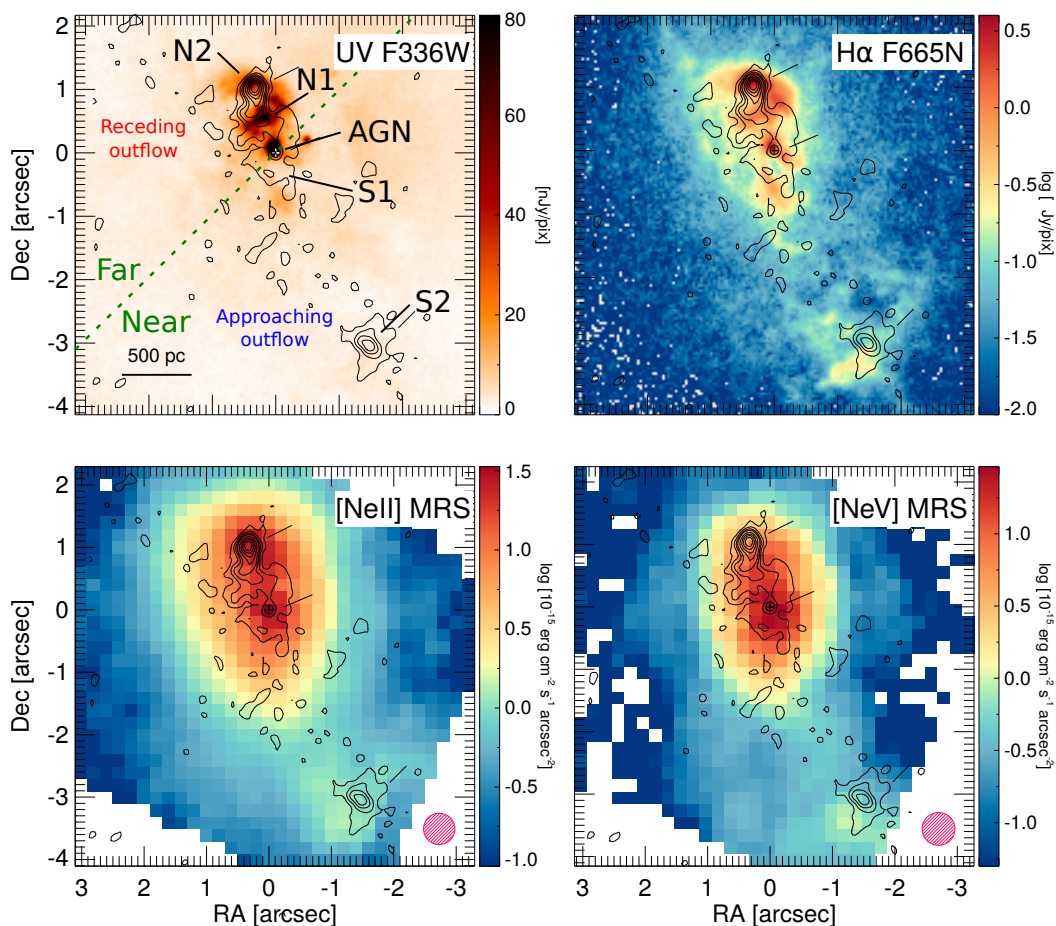


Fig. 1: NGC 7319 near-UV/blue image obtained with the F336W ($\lambda_p=0.335\mu\text{m}$) filter of *HST*/WFC3 (top left); $\text{H}\alpha$ emission from the continuum subtracted *HST*/WFC3 F665N image (top right; Appendix A.2). The bottom panels show the *JWST*/MIRI MRS [Ne II] $12.81\mu\text{m}$ (left) and [Ne V] $14.32\mu\text{m}$ (right) emission line maps (0th moment map). The contours are the MERLIN 1.4 GHz (20 cm) radio emission map from Fig. 7 of Xanthopoulos et al. 2004. The location of the radio hotspots, N2 and S2, and the nuclear diffuse radio lobes, N1 and S1, is indicated in the top left panel. The dashed green line marks the stellar kinematic major axis (Yttergren et al. 2021). The far and near sides of the stellar disk are indicated (see Section 3). The location of the receding (redshifted) and approaching (blueshifted) sides of the ionized outflow are indicated (Rodríguez-Baras et al. 2014; Yttergren et al. 2021). The red hatched circles represent the MIRI MRS PSF FWHM.

measured the first moment (velocity field) and second moment (velocity dispersion, σ) of the line emission profile. Line maps are presented in Figs. 1–4.

We extracted the spectra of 3 regions (AGN, N2, and S2; Figs. 1, 2, and 4) using a $1''$ (~ 450 pc) diameter aperture (~ 2 times the channel 3 PSF FWHM). We applied a point-source correction to the AGN spectrum (see Appendix A.1). For N2 and S2 we did not apply any aperture correction since the emission appears more extended. The spectra are presented in Fig. B.1.

In addition, we used *JWST* and *HST* imaging data to trace the UV, $\text{H}\alpha$, and dust lanes morphologies (see Appendices A.2 and A.3).

3. Jet-ISM interaction in NGC 7319

Interferometric radio observations at 1.4, 5 and, 8 GHz revealed an unresolved core, with a flat radio spectrum, and two synchrotron hotspots at the ends of the radio lobes. The hotspots are asymmetrically located at 430 pc and 1.5 kpc projected distances, respectively, from the core, which implies a high arm-length ratio of ~ 3.5 (Fig. 1 and Aoki et al. 1999; Xanthopoulos et al. 2004). Relativistic beaming can produce asymmetric

arm-length ratios. Assuming intrinsically symmetric jet propagation, the approaching side is brighter and its apparent distance higher (Boettcher et al. 2012). On the contrary, in NGC 7319 the brighter side is closer to the core and coincident with the receding side of the ionized outflow (see below and Fig. 1). Alternatively, the length asymmetry can be produced by the interaction of the northern radio jet with the ISM (e.g., Xanthopoulos et al. 2004).

This galaxy contains a $\sim 400\text{ km s}^{-1}$ ionized gas outflow, detected in [O III] 5007\AA and $\text{H}\alpha$. This outflow is co-spatial with the radio lobes and its kinematic major axis is aligned with the core-hotspots axis (see Yttergren et al. 2021), which suggests that the outflow is driven by the radio jet (Aoki et al. 1996).

Assuming that the large scale spiral pattern and tidal features of NGC 7319 resulting from prograde galaxy interactions are trailing (Renaud et al. 2010), the stellar disk is rotating counter-clockwise. This assumption, together with the stellar kinematics (Yttergren et al. 2021), determines the far and near sides of the disk (see top-left panel of Fig. 1). Therefore, the northern side of the jet (receding outflow) is seen in projection on the far side of the disk, while the southern side (approaching outflow) is over the near side of the disk. This geometry and outflow kinematics is at odds with a perpendicular to the disk jet orientation. Instead

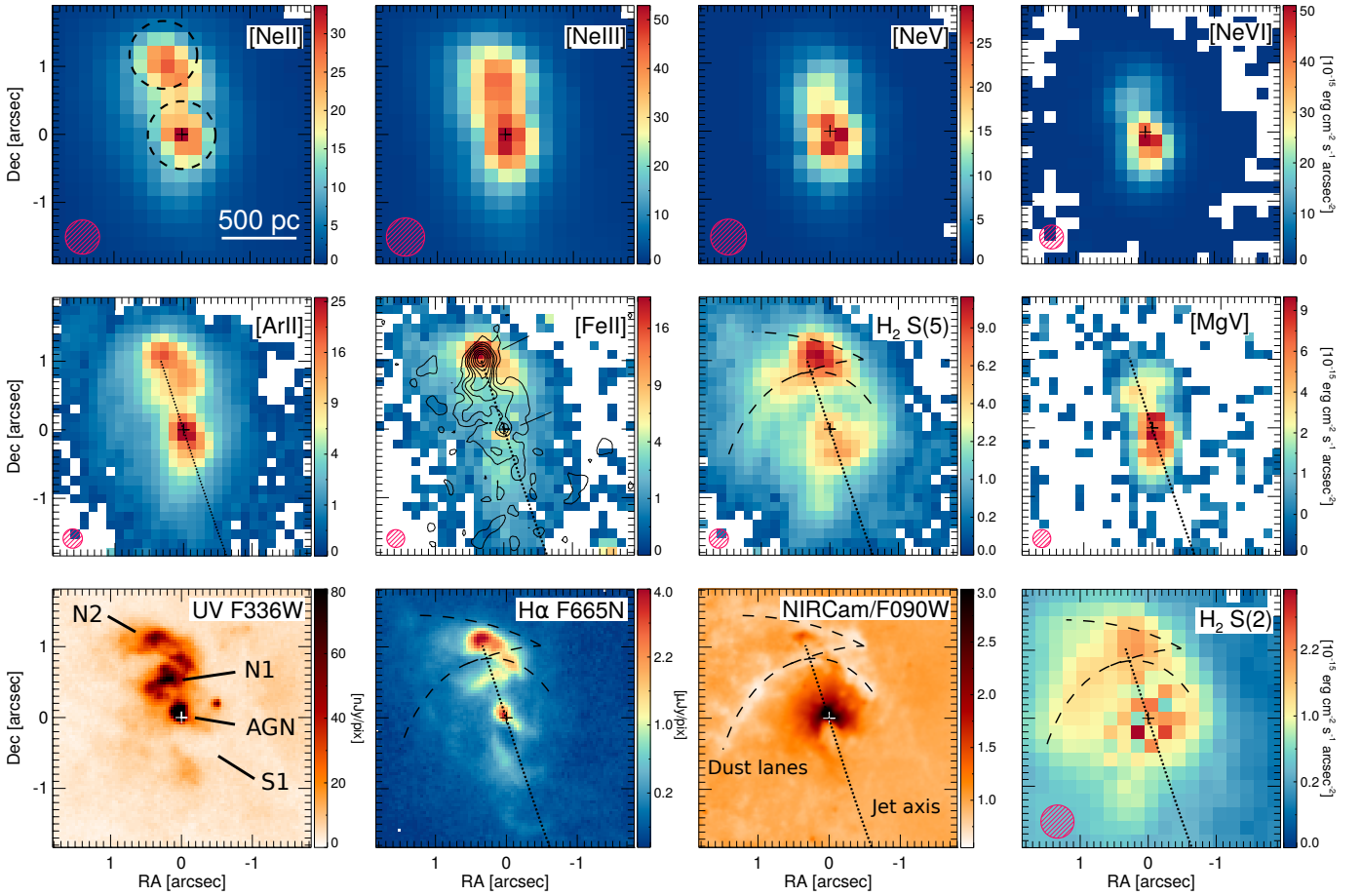


Fig. 2: Central $3'' \times 6''$ region of NGC 7319, which includes the AGN and the northern radio lobe and hotspot N2. First row: from left to right [Ne II] $12.81 \mu\text{m}$, [Ne III] $15.56 \mu\text{m}$, [Ne V] $14.32 \mu\text{m}$, and [Ne VI] $7.65 \mu\text{m}$ MIRI MRS line maps. The dashed circles on the [Ne II] map are the AGN and N2 extraction apertures. Second row: from left to right [Ar II] $6.99 \mu\text{m}$, [Fe II] $5.34 \mu\text{m}$, $\text{H}_2 \text{ S}(5)$ $6.91 \mu\text{m}$, and [Mg V] $5.61 \mu\text{m}$ MIRI MRS line maps. The contours on the second panel represent the 1.4 GHz emission as in Fig. 1. Third row: First two panels are as the top row panels of Fig. 1. The third panel is the *JWST*/NIRCam F090W ($\lambda_p = 0.90 \mu\text{m}$) image after dividing by a Gaussian (FWHM = $1''.2$) smoothed version of itself to highlight finer details. The fourth panel is the $\text{H}_2 \text{ S}(2)$ $12.28 \mu\text{m}$ emission line. The black dotted and dashed lines trace the jet axis (N2 hotspot-AGN axis) and disk dust lanes, respectively. The red hatched circles represent the PSF FWHM, $\sim 0''.26$ – $0''.60$ depending on the wavelength, estimated from the unresolved AGN continuum.

it is consistent with the jet axis being close to the plane of the disk and, therefore, it favors jet-ISM interactions.

The top panels of Fig. 1 show the near-UV/blue continuum and $\text{H}\alpha$ emissions which are spatially coincident with the radio lobes and peak close to the northern hotspot, N2. Bow-shocks are also present at both the northern and southern lobes, especially in the $\text{H}\alpha$ image. The bottom panels show the MRS maps of the [Ne II] $12.81 \mu\text{m}$ (ionization potential, IP = 22 eV) and the high-ionization [Ne V] $14.32 \mu\text{m}$ (IP = 97 eV) emission lines. Both mid-IR lines have morphologies that follow the radio jet axis and resemble that of the higher angular resolution UV/optical imaging data. So they are likely connected to the jet as well. Nevertheless, a contribution to these lines from the AGN extended narrow line region (NLR) is also possible.

3.1. Jet-molecular gas interaction: northern radio hotspot

Fig. 2 shows the line maps centered on the more luminous northern radio lobe. The first row compares the Ne emission from Ne^+ to Ne^{5+} (IP = 126 eV). These maps trace the ionization state of the gas avoiding uncertainties due to relative atomic abundances. We find that the extent of the Ne emission decreases with in-

creasing ionization stage. The lower ionization [Ne II] emission peaks close to N2, with reduced emission at N1 closer to the nucleus. Intermediate [Ne III] emission seems to peak between N1 and N2, while the highest ionization [Ne V] and [Ne VI] lines, instead, are brighter at N1. The latter indicates that the intense UV radiation from N1 is unlikely produced by star-formation. To examine the excitation at higher angular resolution, we use the short wavelength channel 1 [Ar II] $6.99 \mu\text{m}$ (IP = 15.8 eV) and [Mg V] $5.61 \mu\text{m}$ (IP = 109 eV) emission lines as proxies of the low- and high-ionization gas (second row of Fig. 2). The better angular resolution allows us to establish that the high-ionization emission is mostly concentrated at N1 to the north and at S1 to the south of the nucleus, while lower ionization gas dominates the emission at the N2 radio hotspot. The [Ar II] morphology is also similar to that of the $\text{H}\alpha$ map (bottom row).

Radio jets interact with the ISM transferring energy and momentum to the ISM clouds through shock waves (Sutherland & Bicknell 2007). These shock waves enhance the mid-IR rotational H_2 emission in radio galaxies (Guillard et al. 2012; Ogle et al. 2010). In NGC 7319, the $\text{H}_2 \text{ S}(5)$ $6.91 \mu\text{m}$ emission peaks close to the N2 hotspot. Both $\text{H}_2 \text{ S}(2)$ $12.28 \mu\text{m}$ and $\text{H}_2 \text{ S}(5)$ also trace the dust lanes visible in the F090W image (see Fig. 2).

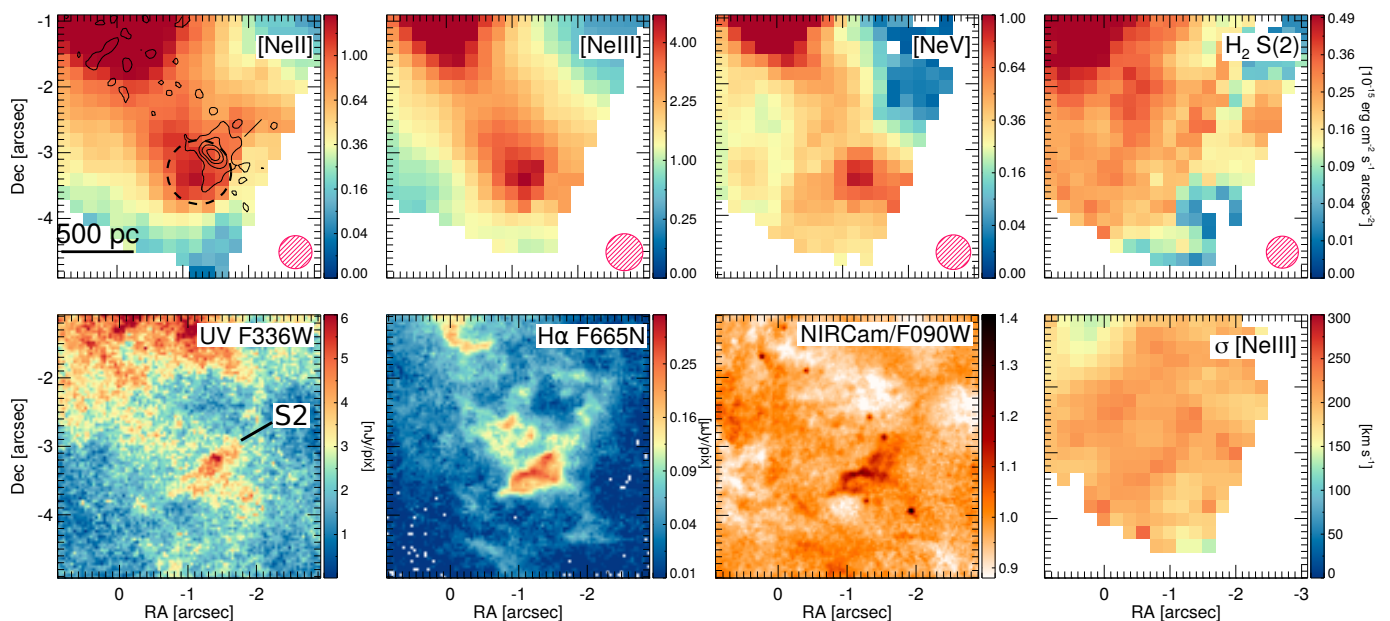


Fig. 4: Southern radio lobe and hotspot S2 of NGC 7319. First row: from left to right [Ne II] 12.81 μm , [Ne III] 15.56 μm , [Ne V] 14.32 μm , and H₂ S(2) 12.28 μm MIRI MRS line maps. The contours on the first panel represent the 1.4 GHz emission for reference as in Fig. 1. The dashed circle on the [Ne II] map is the S2 extraction aperture. The red hatched circles represent the PSF FWHM, $\sim 0''.49$ – $0''.56$. Second row: First three panels are as the last row panels of Fig. 2. The fourth panel is the velocity dispersion of the [Ne III] 15.56 μm emission line.

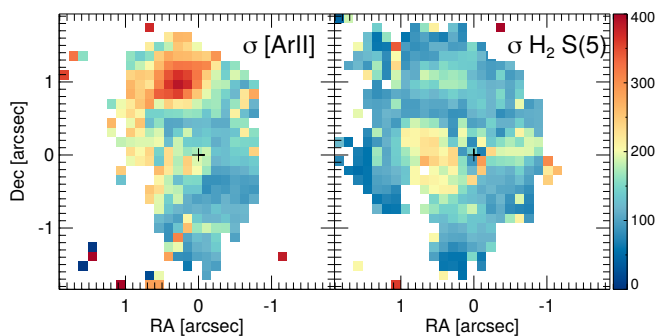


Fig. 3: Velocity dispersion of the [Ar II] 6.99 μm (left) and H₂ S(5) 6.91 μm (right) emission lines. Same field of view as Fig. 2. The velocity field is shown in Fig. C.1.

Therefore, the radio hotspot seems to be located <100 pc away from the intersection between the dust lanes and the jet axis. We note, however, that the contrast between the dust lanes and hotspot emission is smaller for the lower excitation H₂ S(2) transition. The jet-ISM interaction at N2 is also supported by the bright [Fe II] 5.34 μm emission, which is enhanced in shocks (Allen et al. 2008).

The polycyclic aromatic hydrocarbon (PAH) emission at N2 is weak relative to the H₂ lines (Fig. B.1), as seen in shock-excited regions (Guillard et al. 2012; Beirão et al. 2015). The 11.3 μm PAH flux, estimated by subtracting a local continuum and integrating the spectrum between 11.0 and 11.8 μm to S(1) ratio is ~ 2.5 , which is ~ 10 times lower than in local starburst galaxies (see Pereira-Santaella et al. 2010a). Therefore, photodissociation region (PDR) excitation at N2 is unlikely. In addition, the 7.7 μm PAH feature is extremely weak at N2 (Fig. B.1) and only the 11.3 μm PAH, which is more resilient in hard environments (García-Bernete et al. 2022), is clearly detected. Similar spectra are seen in radio galaxies with strong jets which dif-

fer from star-forming galaxies where the 7.7 μm PAH feature is dominant (Ogle et al. 2010; Zakamska et al. 2016; Smith et al. 2007).

The ionized gas velocity dispersion, i.e. turbulence, is increased at N2 ($\sigma \sim 300$ km s⁻¹). The σ of the rotational H₂ transitions (~ 150 km s⁻¹) however is not enhanced (Fig. 3 and Table B.1), which is consistent with observations of radio galaxies (Guillard et al. 2012).

Low-power jets ($P_{\text{jet}} < 10^{43}$ erg s⁻¹) cannot easily pierce dense gas clouds and might remain trapped in the ISM (Mukherjee et al. 2016). We estimate $P_{\text{jet}} \sim 2 \times 10^{43}$ erg s⁻¹ (Sect. 4), so this could be the case for the northern lobe which was decelerated by molecular clouds in the disk.

3.2. Jet-atomic gas interaction: southern radio hotspot

The more distant southern lobe was only observed with the longer wavelength MRS channels 3 and 4 due to the larger FoV at those wavelengths. For this reason, a reduced set of mid-IR lines is available (Fig. 4). The three Ne lines peak at the same location close to the S2 radio hotspot, although, we note that the offset between the Ne and radio peaks is larger at S2 than at N2 ($0''.2$ vs. $0''.5$). In the higher spatial resolution *HST* and NIRCam continuum and H α images, this region appears as an arc/bow-shock. This structure was already identified by Aoki et al. (1999). The velocity dispersion of the ionized gas is high, ~ 220 – 300 km s⁻¹ (Table B.1), and similar to that of N2, although the S2 hotspot does not stand out in the velocity dispersion map (last panel of Fig. 4). Contrary to the N2 hotspot, at S2 the H₂ emission is not enhanced, although in this case the S(5) line, more sensitive to the jet-excited molecular gas, is not available. The higher H₂ S(1) to S(2) ratio in this region also supports a lower excitation of the molecular gas in S2 (Table 1). Conversely, the higher [Ne III] and [Ne V] to [Ne II] ratios indicate that the ionized gas phase is more highly ionized in S2 (Table 1). Therefore,

Table 1: MIRI/MRS line ratios

Ratio	AGN	N2	S2
[Ne III]/[Ne II]	2.08	1.16	3.31
[Ne V]/[Ne II]	0.96	0.22	0.60
[Ne V]/[Ne III]	0.46	0.19	0.18
[Ne V]/H ₂ S(1)	10.6	1.85	1.43
H ₂ S(1)/H ₂ S(2)	0.92	1.27	2.70

Notes. Line ratios between the [Ne II]12.81 μm , [Ne III]15.56 μm , [Ne V]14.32 μm , H₂ S(1), and H₂ S(2) emission lines. All the lines are observed with the MRS channel 3. The estimated ratio uncertainty, based on the flux uncertainties, is $\sim 10\%$ (see Table B.1). AGN Ne line ratios are similar to the median ratios measured in local Seyfert galaxies (Pereira-Santaella et al. 2010b).

these results suggest that the jet is interacting more strongly with the atomic gas phase, relative to the molecular, at S2 than at N2.

4. Ionized and warm/hot molecular gas mass affected by the jet

We derive the ionized gas mass using Eq. 1 of Venturi et al. (2021). The ratio between H α and H I 6–5 7.46 μm (Pf α) is 112 at 10 000 K (Storey & Hummer 1995). We assume that the electron density, n_e , in the ionized gas in the shock is between 100 cm^{-3} and the upper limit, $n_e < 500 \text{ cm}^{-3}$, obtained from the [Fe II]5.34 μm /[Fe II]4.89 μm >60 ratio (Fig. D.1). The resulting mass range is $M_{\text{ion}} = (2.4\text{--}12) \times 10^5 M_{\odot}$.

The warm/hot molecular gas mass at N2 is derived using the H₂ S(1) to S(8) transitions. The critical densities of these transitions are relatively low, $n_{\text{H}_2} = 10^2$ to 10^5 cm^{-3} at 500 K (Le Bourlot et al. 1999), so we can assume local thermodynamic equilibrium (LTE) conditions. Under this assumption, the S(1) to S(6) transitions can be fit with a two temperature model: a warm component with $T_w = 330 \pm 40 \text{ K}$ and $M_{\text{H}_2, w} = (6.0 \pm 1.4) \times 10^5 M_{\odot}$ which dominates the S(1) and S(2) emission; and a hotter component with $T_h = 900 \pm 60 \text{ K}$ and $M_{\text{H}_2, h} = (0.44 \pm 0.12) \times 10^5 M_{\odot}$ which dominates the S(3)–S(6) emission (Fig. 5). The higher J transitions S(7) and S(8) deviate from this fit suggesting the existence of a hotter component, whose temperature is $> 1000 \text{ K}$ but not well constrained by these transitions alone.

Molecular gas is expected to reform in post-shock regions (Hollenbach & McKee 1989). However, the lower H₂ velocity dispersion compared to that of the ionized gas (Fig. 3), suggests that the origin of the H₂ emission are not reformed H₂ molecules after the cooling of that ionized gas. Instead, it is plausible that this H₂ was already present and it is being excited by the jet/shocks.

The ionized gas velocity dispersion is ~ 2 times higher than that of the warm H₂ and the $M_{\text{ion}}/M_{\text{H}_2, w}$ ratio is $\sim 0.3\text{--}2.5$. Therefore, the mechanical energy of the ionized phase, $E_{\text{ion}} = M_{\text{ion}} \sigma^2 / 2 = (0.2\text{--}1.1) \times 10^{54} \text{ erg}$, is $\sim 1.3\text{--}10$ times higher than that of the warm H₂, $E_{\text{H}_2, w} = (0.13 \pm 0.03) \times 10^{54} \text{ erg}$.

We estimate a jet cavity power of $P_{\text{jet}} \sim 2 \times 10^{43} \text{ erg s}^{-1}$ using Eq. 16 of Bîrzan et al. (2008) and $L_{1.4 \text{ GHz}} = 3.3 \times 10^{22} \text{ W Hz}^{-1}$ (Aoki et al. 1999), which is similar to NGC 1068 (García-Burillo et al. 2014). The ratio $(E_{\text{H}_2, w} + E_{\text{ion}}) / (t_{\text{jet}} P_{\text{jet}})$ is $\sim (0.4\text{--}1.6) \times 10^{-3}$, where the jet life, $t_{\text{jet}} \sim 1.1 \times 10^6 \text{ yr}$, is estimated from the jet travel time to S2 following Venturi et al. (2021). This indicates that only a small fraction of the jet energy ($< 0.2\%$) remains as mechanical energy in the ionized and warm molecular ISM phases. We note that the jet can also transfer

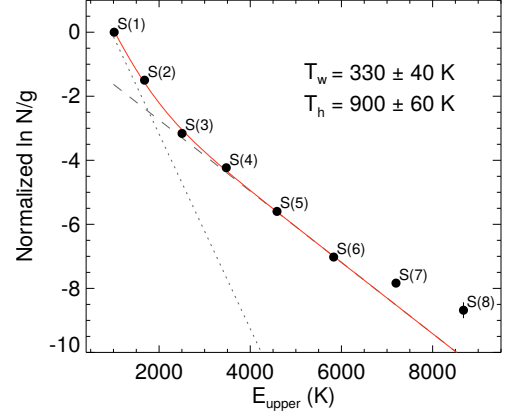


Fig. 5: Rotational diagram showing the H₂ 0–0 S(1) to S(8) transitions measured at the northern radio hotspot N2 assuming an ortho-to-para ratio of 3 expected for $T_{\text{rot}} > 200 \text{ K}$ (Burton et al. 1992). The red line is the best LTE fit with 2 temperatures to the S(1)–S(6) lines. The dotted (dashed) line represents the warm (hot) component. The solid red line is the sum of the two components.

mechanical energy to the cold molecular gas traced by CO and launch molecular outflows (e.g., Morganti et al. 2015; Ramos Almeida et al. 2022).

5. Summary and conclusions

We analyzed the low-power ($L_{1.4 \text{ GHz}} = 3.3 \times 10^{22} \text{ W Hz}^{-1}$) jet-ISM interaction in the Seyfert 2 galaxy NGC 7319 using *JWST*/MIRI MRS data. We find evidence suggesting that molecular gas in dust lanes decelerates the jet at the northern hotspot, N2, which is 3 times closer to the nucleus than the southern hotspot, S2. Enhanced warm/hot H₂ emission ($T_{\text{H}_2} \sim 330 \text{ K}$ and 900 K) as well ionized gas tracers, and [Fe II]5.34 μm emission, which is a shock tracer, is detected at N2 at the intersection between the jet axis and dust lanes. On the contrary, at the more distant S2 hotspot, the H₂ excitation is lower and the atomic gas is more highly ionized. This suggests that the jet interacts more strongly with the atomic gas there. Therefore, the reduced molecular gas-jet interaction at the southern radio lobe could make it easier for the jet reach greater distances.

Extended (distances up to 1.5 kpc from the nucleus) high-ionization ([Mg V]5.61 μm , [Ne VI]7.65 μm , [Ne V]14.32 μm , and [Ne V]24.32 μm) emission is detected close to the radio jet hotspots. These lines can be produced in the photoionized precursor of the shock-waves produced by the jet, or photoionized by the AGN radiation in an extended NLR.

At N2, $M_{\text{ion}} = (2.4\text{--}12) \times 10^5 M_{\odot}$ is comparable to the warm ($\sim 330 \text{ K}$) H₂ gas mass and > 5 times higher than the hot ($\sim 900 \text{ K}$) H₂ mass. The ionized gas is also more turbulent ($\sigma_{\text{ion}} \sim 300 \text{ vs. } \sigma_{\text{H}_2} \sim 150 \text{ km s}^{-1}$). Therefore, the mechanical energy of the ionized gas is $\sim 1.3\text{--}10$ times higher than that of the warm+hot molecular gas. From these estimates, we find that $< 0.2\%$ of the jet energy remains as mechanical energy in these two ISM phases.

These initial results show the *JWST*/MIRI MRS capabilities to constrain the AGN/jet feedback on the multiphase ISM at unprecedented sensitivity, and angular and spectral resolutions in the mid-IR.

Acknowledgements. We thank P. Gandhi and E. Hicks for the careful reading of the manuscript and useful discussion. The authors acknowledge the ERO team for developing their observing program with a zero-exclusive-access period. MPS acknowledges support from the Comunidad de Madrid through the Atracción de Talento Investigador Grant 2018-T1/TIC-11035 and PID2019-105423GA-I00 (MCIU/AEI/FEDER,UE). JAM, AL, and LC acknowledge support by grant PIB2021-127718NB-I00 by the Spanish Ministry of Science and Innovation/State Agency of Research (MCIN/AEI). IGB acknowledges support from STFC through grant ST/S000488/1. AAH acknowledges support from grant PGC2018-094671-B-I00 funded by MCIN/AEI/10.13039/501100011033 and by ERDF A way of making Europe. SGB acknowledges support from the research project PID2019-106027GA-C44 of the Spanish Ministerio de Ciencia e Innovación. CRA acknowledges support from grant PID2019-106027GB-C42, funded by MICINN-AEI/10.13039/501100011033, from EUR2020-112266, funded by MICINN-AEI/10.13039/501100011033 and the European Union NextGenerationEU/PRTR, and from the Consejería de Economía, Conocimiento y Empleo del Gobierno de Canarias and the European Regional Development Fund (ERDF) under grant ProID2020010105, ACCISI/FEDER, UE. This work is based on observations made with the NASA/ESA/CSA James Webb Space Telescope. The data were obtained from the Mikulski Archive for Space Telescopes at the Space Telescope Science Institute, which is operated by the Association of Universities for Research in Astronomy, Inc., under NASA contract NAS 5-03127 for JWST; and from the European JWST archive (eJWST) operated by the ESAC Science Data Centre (ESDC) of the European Space Agency. These observations are associated with program #2732, #1049, #1050. This research is based on observations made with the NASA/ESA Hubble Space Telescope obtained from the Space Telescope Science Institute, which is operated by the Association of Universities for Research in Astronomy, Inc., under NASA contract NAS 5-26555. These observations are associated with programs 11502 and 12301.

References

- Alatalo, K., Blitz, L., Young, L. M., et al. 2011, *ApJ*, 735, 88
- Allen, M. G., Groves, B. A., Dopita, M. A., Sutherland, R. S., & Kewley, L. J. 2008, *ApJS*, 178, 20
- Alonso-Herrero, A., Pereira-Santaella, M., García-Burillo, S., et al. 2018, *ApJ*, 859, 144
- Aoki, K., Kosugi, G., Wilson, A. S., & Yoshida, M. 1999, *ApJ*, 521, 565
- Aoki, K., Ohtani, H., Yoshida, M., & Kosugi, G. 1996, *AJ*, 111, 140
- Argyriou, I., Wells, M., Glasse, A., et al. 2020, *A&A*, 641, A150
- Beirão, P., Armus, L., Lehnert, M. D., et al. 2015, *MNRAS*, 451, 2640
- Bîrzan, L., McNamara, B. R., Nulsen, P. E. J., Carilli, C. L., & Wise, M. W. 2008, *ApJ*, 686, 859
- Boettcher, M., Harris, D. E., & Krawczynski, H. 2012, *Relativistic Jets from Active Galactic Nuclei*
- Burton, M. G., Hollenbach, D. J., & Tielens, A. G. G. 1992, *ApJ*, 399, 563
- Dasyra, K. M., Combes, F., Novak, G. S., et al. 2014, *A&A*, 565, A46
- Davé, R., Anglés-Alcázar, D., Narayanan, D., et al. 2019, *MNRAS*, 486, 2827
- Fernández-Ontiveros, J. A., Dasyra, K. M., Hatziminaoglou, E., et al. 2020, *A&A*, 633, A127
- Gao, Y. & Xu, C. 2000, *ApJ*, 542, L83
- García-Bernete, I., Alonso-Herrero, A., García-Burillo, S., et al. 2021, *A&A*, 645, A21
- García-Bernete, I., Rigopoulou, D., Alonso-Herrero, A., et al. 2022, *MNRAS*, 509, 4256
- García-Burillo, S., Combes, F., Ramos Almeida, C., et al. 2019, *A&A*, 632, A61
- García-Burillo, S., Combes, F., Usero, A., et al. 2014, *A&A*, 567, A125
- Guillard, P., Ogle, P. M., Emonts, B. H. C., et al. 2012, *ApJ*, 747, 95
- Hollenbach, D. & McKee, C. F. 1989, *ApJ*, 342, 306
- Kramida, A., Yu. Ralchenko, Reader, J., & and NIST ASD Team. 2021, NIST Atomic Spectra Database (ver. 5.9), [Online]. Available: <https://physics.nist.gov/asd> [2022, July 27]. National Institute of Standards and Technology, Gaithersburg, MD.
- Labiano, A., Argyriou, I., Álvarez-Márquez, J., et al. 2021, *A&A*, 656, A57
- Le Bourlot, J., Pineau des Forêts, G., & Flower, D. R. 1999, *MNRAS*, 305, 802
- Luridiana, V., Morisset, C., & Shaw, R. A. 2015, *A&A*, 573, A42
- Morganti, R., Oosterloo, T., Oonk, J. B. R., Frieswijk, W., & Tadhunter, C. 2015, *A&A*, 580, A1
- Mukherjee, D., Bicknell, G. V., Sutherland, R., & Wagner, A. 2016, *MNRAS*, 461, 967
- Ogle, P., Boulanger, F., Guillard, P., et al. 2010, *ApJ*, 724, 1193
- Pereira-Santaella, M., Alonso-Herrero, A., Rieke, G. H., et al. 2010a, *ApJS*, 188, 447
- Pereira-Santaella, M., Diamond-Stanic, A. M., Alonso-Herrero, A., & Rieke, G. H. 2010b, *ApJ*, 725, 2270
- Ramos Almeida, C., Bischetti, M., García-Burillo, S., et al. 2022, *A&A*, 658, A155
- Renaud, F., Appleton, P. N., & Xu, C. K. 2010, *ApJ*, 724, 80
- Ricci, C., Trakhtenbrot, B., Koss, M. J., et al. 2017, *ApJS*, 233, 17
- Rieke, G. H., Ressler, M. E., Morrison, J. E., et al. 2015, *PASP*, 127, 665
- Rigby, J., Perrin, M., McElwain, M., et al. 2022, *arXiv e-prints*, arXiv:2207.05632
- Rodríguez-Baras, M., Rosales-Ortega, F. F., Díaz, A. I., Sánchez, S. F., & Pasquali, A. 2014, *MNRAS*, 442, 495
- Smith, J. D. T., Draine, B. T., Dale, D. A., et al. 2007, *ApJ*, 656, 770
- Smyth, R. T., Ramsbottom, C. A., Keenan, F. P., Ferland, G. J., & Ballance, C. P. 2019, *MNRAS*, 483, 654
- Storey, P. J. & Hummer, D. G. 1995, *MNRAS*, 272, 41
- Sulentic, J. W., Rosado, M., Dultzin-Hacyan, D., et al. 2001, *AJ*, 122, 2993
- Sutherland, R. S. & Bicknell, G. V. 2007, *ApJS*, 173, 37
- Venturi, G., Cresci, G., Marconi, A., et al. 2021, *A&A*, 648, A17
- Weinberger, R., Springel, V., Hernquist, L., et al. 2017, *MNRAS*, 465, 3291
- Wells, M., Pel, J.-W., Glasse, A., et al. 2015, *PASP*, 127, 646–664
- Williams, B. A., Yun, M. S., & Verdes-Montenegro, L. 2002, *AJ*, 123, 2417
- Wright, G. S., Wright, D., Goodson, G. B., et al. 2015, *PASP*, 127, 595
- Xanthopoulos, E., Muxlow, T. W. B., Thomasson, P., & Garrington, S. T. 2004, *MNRAS*, 353, 1117
- Yttergren, M., Misquitta, P., Sánchez-Monge, Á., et al. 2021, *A&A*, 656, A83
- Zakamska, N. L., Lampayan, K., Petric, A., et al. 2016, *MNRAS*, 455, 4191

¹ Centro de Astrobiología (CSIC-INTA), Ctra de Torrejón a Ajalvir, km 4, 28850, Torrejón de Ardoz, Madrid, Spain

² Observatorio Astronómico Nacional (OAN-IGN)-Observatorio de Madrid, Alfonso XII, 3, 28014, Madrid, Spain
e-mail: miguel.pereira@oan.es

³ Department of Physics, University of Oxford, Keble Road, Oxford OX1 3RH, UK

⁴ Telespazio UK for the European Space Agency, ESAC, Camino Bajo del Castillo s/n, 28692 Villanueva de la Cañada, Spain

⁵ Centro de Astrobiología (CSIC-INTA), ESAC Campus, E-28692 Villanueva de la Cañada, Madrid, Spain

⁶ Departamento de Física de la Tierra y Astrofísica, Fac. de CC Físicas, Universidad Complutense de Madrid, 28040, Madrid, Spain

⁷ Instituto de Física de Partículas y del Cosmos IPARCOS, Fac. CC Físicas, Universidad Complutense de Madrid, 28040 Madrid, Spain

⁸ Department of Physics & Astronomy, University of Southampton, Hampshire, SO17 1BJ, Southampton, UK

⁹ Instituto de Astrofísica de Canarias, Calle Vía Láctea, s/n, 38205 La Laguna, Tenerife, Spain

¹⁰ Departamento de Astrofísica, Universidad de La Laguna, 38206, La Laguna, Tenerife, Spain

¹¹ School of Mathematics, Statistics and Physics, Newcastle University, NE1 7RU, Newcastle upon Tyne, UK

Appendix A: Data reduction

Appendix A.1: MIRI/MRS data reduction

MIRI/MRS covers the mid-IR spectral range between 4.9 and 28.1 μm . This spectral range is split into four channels (channel 1 from 4.9 to 7.65 μm ; channel 2 from 7.51 to 11.71 μm ; channel 3 from 11.55 to 18.02 μm ; and channel 4 from 17.71 to 28.1 μm). Each channel is in turn divided into three sub-bands (short, medium, and long) that cover a third of the channel spectral range. A single exposure simultaneously observes a single sub-band for the four channels. The field of view (FoV) and pixel size are smaller for the shorter wavelength channels (from 3'' \times 3'' \times 7'' FoV and \sim 0''2 pixel in channel 1 to 6'' \times 6'' \times 7''6 FoV and \sim 0''3 pixel in channel 4) to better sample the diffraction limited *JWST* point spread function (PSF; see Rieke et al. 2015; Wells et al. 2015; Wright et al. 2015).

We downloaded the NGC 7319 uncalibrated data from the *JWST* archive. The MIRI/MRS observations were processed using the *JWST* calibration pipeline (release 1.6.3) with the context 0939 of the Calibration References Data System (CRDS). We followed the standard pipeline procedure to generate the fully calibrated detector products (level 2b) for the on-source and background observations (see Álvarez-Márquez et al. in prep. for a more comprehensive explanation of the MRS calibration data process). Before generating the 3D MRS spectral cubes, we applied a residual fringe correction in the detector plane¹. This step corrects the low frequency fringe residuals remaining after the standard pipeline fringe flat correction. (Argyriou et al. 2020, Gasman et al. in prep., Kavanagh et al. in prep.).

Then, we generated the twelve 3D spectral cubes (the three sub-bands, short, medium, and long bands, for the four MRS channels) with the default spatial and spectral samplings. We estimated the background emission by calculating the median value for each wavelength channel in the background data cubes. This median value for each spectral channel was subtracted to on-source data cubes.

For the nuclear spectra of the AGN, an additional residual fringe correction was implemented to correct for the high frequency fringes generated in the dichroics which are noticeable in the spectra of bright point sources in channels 3 and 4. With this final corrections the final fringe residuals are reduced to levels lower than 6%, and a median level of 2-4% (Kavanagh et al. in prep.).

From the emission line fits, we estimate that the current MRS wavelength calibration has, in general, offsets smaller than $\pm 100 \text{ km s}^{-1}$, consistent with the *JWST* commissioning report (Rigby et al. 2022), except for the medium sub-band of channel 3 (13.29–15.52 μm) where a constant shift of $\sim 0.04 \mu\text{m}$ ($\sim 900 \text{ km s}^{-1}$) is present, and the medium sub-band of channel 2 (8.67–10.15 μm) where the wavelength shift is variable. In addition, the wavelength solution of the long sub-band of channel 3 around $\sim 17.3 \mu\text{m}$ (observed wavelength of the $\text{H}_2 \text{ S}(1)$ transition in NGC 7319), is affected by artifacts which alter the line profile by creating spurious double peaked profiles at some positions of the data cube but they do not alter the integrated line flux. These issues have been identified and they do not affect the analysis presented in this work.

The unresolved line full-width half-maximum ($\text{FWHM}=c/\text{resolving power}$) increases from $\pm 80 \text{ km s}^{-1}$ to 130 km s^{-1} with increasing wavelength for the channels analyzed here (1, 2, and 3; Labiano et al. 2021, Jones et al. in prep.). Therefore, all the

emission lines in NGC 7319, which have $\text{FWHM}/2.35=\sigma=130\text{--}370 \text{ km s}^{-1}$ (Table B.1), are spectrally resolved.

We estimated the point-source correction for a 1'' diameter aperture using the MRS observations of HD 163466 (Program ID #1050) for channels 1, 2, and 3, and SMP-LMC-058 (Program ID #1049) for channel 4.

Appendix A.2: Ancillary *JWST* and *HST* imaging

JWST/NIRCam and MIRI wide-band filter images are also available as part of the ERO data release. We obtained the calibrated level 3 images (pipeline release 1.5.3 and context 0919 of the CRDS) from the *JWST* archive. We used the NIRCam F090W ($\lambda_p=0.90 \mu\text{m}$; $\Delta\lambda=0.19 \mu\text{m}$)², and the MIRI F1000W ($\lambda_p=10.0 \mu\text{m}$; $\Delta\lambda=2.0 \mu\text{m}$)³ images, which we used to determine the coordinates of the AGN mid-IR emission (Appendix A.3).

Hubble Space Telescope (*HST*) Wide Field Camera 3 (WFC3) images were also retrieved from the Hubble Legacy Archive: the F336W ($\lambda_p=0.335 \mu\text{m}$; $\Delta\lambda=0.051 \mu\text{m}$)⁴, which covers the near-UV/blue emission of the galaxy; and the F665N ($\lambda_p=0.666 \mu\text{m}$; $\Delta\lambda=0.013 \mu\text{m}$), which includes the $\text{H}\alpha$ emission and the weakest line, 6548 Å, of the [N II] doublet at the redshift of NGC 7319. We subtracted the underlying continuum by linear interpolating the F606W ($\lambda_p=0.59 \mu\text{m}$; $\Delta\lambda=0.22 \mu\text{m}$) and F814W ($\lambda_p=0.80 \mu\text{m}$; $\Delta\lambda=0.16 \mu\text{m}$) images at the mean wavelength of the F665N filter, taking into account that the F606W image includes the F665N emission. The [N II]6548 Å/ $\text{H}\alpha$ ratio is <0.3 in the central $\sim 10''$, based on optical integral field spectroscopy (Rodríguez-Baras et al. 2014), so the continuum subtracted F665N morphology is likely dominated by the $\text{H}\alpha$ emission.

Appendix A.3: Astrometric registration

To allow for morphology comparisons between the MRS line maps and the *JWST* and *HST* ancillary images (Appendix A.2), we require relative astrometric differences smaller than 0.06'' (channel 1 data cube half pixel). To achieve this, we registered all the images and line maps to a common frame. We used as reference the Near Infrared Camera (NIRCam) F090W image. The background quasar J223603.7+335824 located 8'' south of the nucleus, and well detected in all the images, was used to align them. The mid-IR AGN coordinates were derived from the F1000W MIRI image. These coordinates were then assigned to the location of the mid-IR AGN continuum peak derived for each of the MRS line maps.

² <https://jwst-docs.stsci.edu/jwst-near-infrared-camera/nircam-instrumentation/nircam-filters>

³ <https://jwst-docs.stsci.edu/jwst-mid-infrared-instrument/miri-instrumentation/miri-filters-and-dispersers>

⁴ <https://hst-docs.stsci.edu/wfc3ihb/chapter-6-uvis-imaging-with-wfc3/6-5-uvis-spectral-elements>

¹ https://jwst-pipeline.readthedocs.io/en/latest/jwst/residual_fringe/index.html.

Appendix B: MIRI/MRS emission lines

Table B.1: MIRI/MRS emission lines

Transition	λ_{rest}	IP ^a	$\log n_{\text{crit}}^b$	AGN		N2		S2		
	μm			eV	cm^{-3}	Flux $10^{-16} \text{ erg cm}^{-2} \text{ s}^{-1}$	σ km s^{-1}	Flux $10^{-16} \text{ erg cm}^{-2} \text{ s}^{-1}$	σ km s^{-1}	Flux $10^{-16} \text{ erg cm}^{-2} \text{ s}^{-1}$
MIRI/MRS Channel 1										
[Fe II]	4.889	7.9	4.39	<1.45	...	<0.87
H ₂ 0–0 S(8)	5.053	4.2 ± 1.1	...	5.5 ± 1.2
[Fe II]	5.340	7.9	3.09	27.5 ± 1.4	253 ± 47	51.27 ± 0.44	336 ± 6
[Fe VII]	5.447	124	6.41	14.13 ± 0.63	...	<0.69
[Mg VII]	5.503	186	6.53	19.5 ± 1.5	...	<0.70
H ₂ 0–0 S(7)	5.511	19.1 ± 2.3	...	19.02 ± 0.40	134 ± 16
[Mg V]	5.610	109	6.60	34.5 ± 1.3	168 ± 49	3.43 ± 0.33
H ₂ 0–0 S(6)	6.109	6.11 ± 0.65	...	6.58 ± 0.49
[Ni II]	6.636	7.6	5.92	<0.68	...	2.74 ± 0.23	241 ± 69
[Fe II]	6.721	7.9	3.09	<1.70	...	1.79 ± 0.23	222 ± 67
H ₂ 0–0 S(5)	6.909	34.8 ± 1.0	196 ± 37	33.05 ± 0.28	144 ± 17
[Ar II]	6.985	15.8	5.62	87.1 ± 1.8	176 ± 24	48.97 ± 0.27	328 ± 3
[Na III]	7.318	47.3	6.80	8.6 ± 1.1	321 ± 71	2.73 ± 0.18	367 ± 38
MIRI/MRS Channel 2										
H I 6–5	7.460	7.2 ± 1.2	...	2.89 ± 0.34	307 ± 75
[Ne VI]	7.652	126	5.80	208.4 ± 1.6	127 ± 15	12.48 ± 0.23	193 ± 22
[Fe VII]	7.814	99.0	6.10	7.0 ± 1.6	...	<0.39
[Ar V]	7.902	59.6	5.20	11.62 ± 0.85	...	1.03 ± 0.23
H ₂ 0–0 S(4)	8.026	15.7 ± 1.0	195 ± 58	14.44 ± 0.21	178 ± 26
[Ar III]	8.991	27.6	5.28	62.5 ± 1.1	128 ± 16	19.02 ± 0.29	264 ± 12
[Mg VII]	9.009	186	5.87	<2.76
[Fe VII]	9.527	99.0	5.74	9.73 ± 0.78	...	2.27 ± 0.17	298 ± 77
H ₂ 0–0 S(3)	9.665	39.25 ± 0.96	200 ± 38	33.05 ± 0.29	170 ± 13
[S IV]	10.51	34.9	4.75	220.0 ± 1.9	138 ± 16	49.94 ± 0.41	260 ± 6
MIRI/MRS Channel 3										
H ₂ 0–0 S(2)	12.28	22.06 ± 0.92	299 ± 27	10.51 ± 0.13	141 ± 16	1.30 ± 0.18
H I 7–6	12.37	<1.51	...	1.01 ± 0.10	327 ± 70	<0.20
[Ne II]	12.81	21.6	5.80	222.1 ± 3.3	171 ± 23	112.8 ± 1.0	311 ± 6	8.36 ± 0.14	239 ± 25	...
[Ar V]	13.10	59.6	4.47	17.1 ± 1.5	...	1.84 ± 0.21	...	<0.23
[Mg V]	13.52	109	5.70	<2.75	...	<0.22	...	<0.13
[Ne V]	14.32	97.2	4.51	213.4 ± 1.4	126 ± 9	24.70 ± 0.17	...	5.03 ± 0.06	149 ± 9	...
[Cl II]	14.37	13.0	4.59	<3.66	...	1.64 ± 0.12	...	<0.16
[Ne III]	15.56	41.0	5.32	462.5 ± 3.2	154 ± 12	131.3 ± 1.1	280 ± 7	27.68 ± 0.33	191 ± 29	...
H ₂ 0–0 S(1)	17.03	20.2 ± 2.4	...	13.35 ± 0.66	...	3.52 ± 0.21
MIRI/MRS Channel 4										
[Fe II]	17.94	7.9	4.39	12.1 ± 2.1	311 ± 97	8.35 ± 0.21	366 ± 15	<0.33
[S III]	18.71	23.3	4.07	218.5 ± 1.8	141 ± 18	60.43 ± 0.63	242 ± 10	12.17 ± 0.25	202 ± 34	...
[Ne V]	24.32	97.2	3.77	312.3 ± 10.4	178 ± 47	23.81 ± 0.34	194 ± 29	5.27 ± 0.41
[O IV]	25.89	54.9	4.00	1167.2 ± 4.9	...	127.1 ± 1.1	...	48.45 ± 0.92	191 ± 8	...
[Fe II]	25.99	7.9	3.95	42.4 ± 4.3	...	11.93 ± 0.67	...	<1.90

Notes. Flux (0th moment) and velocity dispersion (2nd moment; σ) measured at the AGN, N2, and S2 regions. The diameter of the apertures is 1''. A point-source aperture correction is applied to the AGN spectra. The quoted uncertainties are 1σ statistical uncertainties. The absolute calibration uncertainty is $\sim 10\%$ (Rigby et al. 2022). For the non-detections we list the 3σ upper limits for a line with a width of $\sim 200 \text{ km s}^{-1}$. ^(a) Ionization potential of the transition defined as the energy needed to reach the ionization stage producing that transition (Kramida et al. 2021). ^(b) Critical density at $T = 10000 \text{ K}$ for collisions with e^- calculated using PyNeb v1.1.15 (Luridiana et al. 2015).

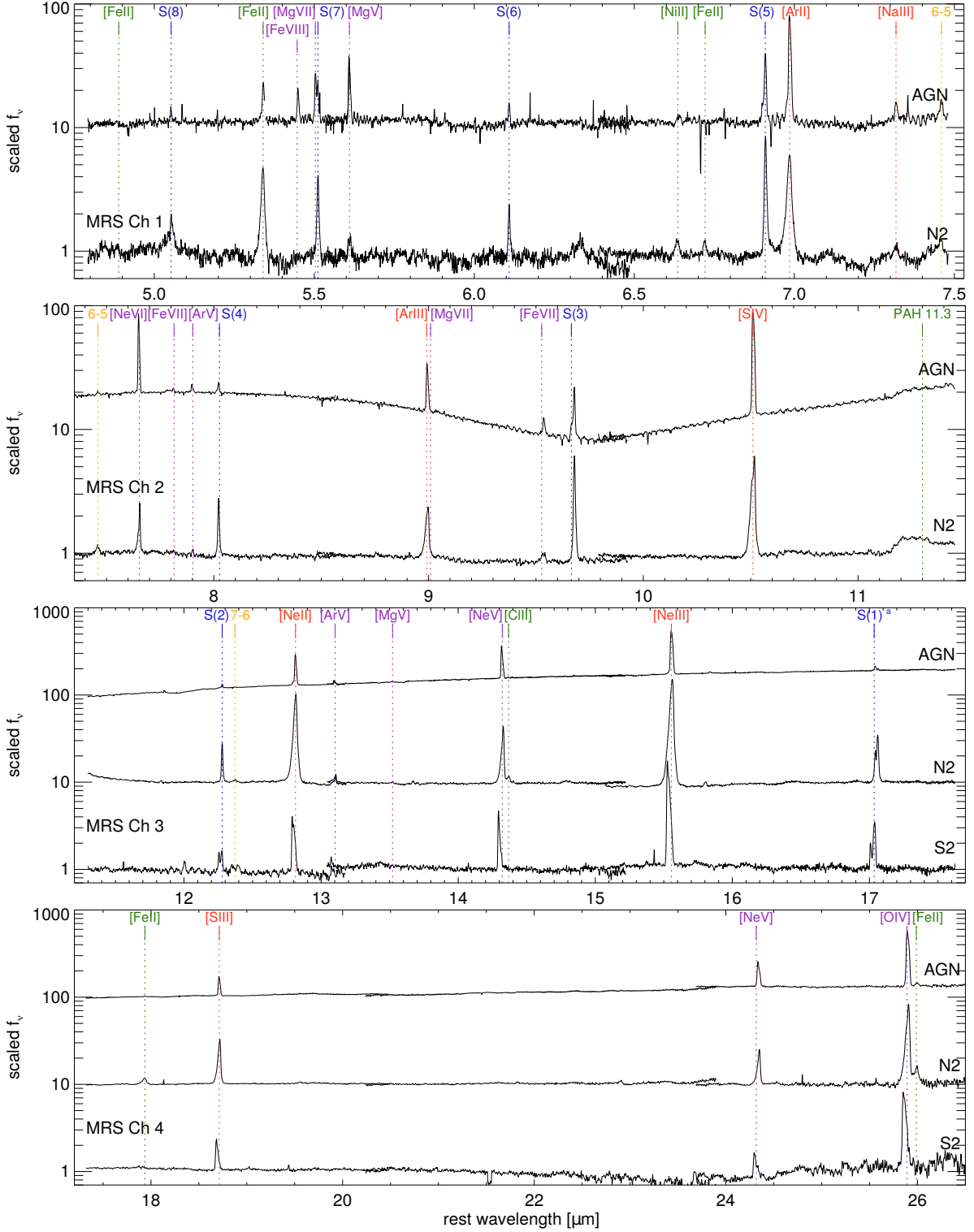


Fig. B.1: Continuum subtracted MIRI/MRS spectra of three regions (AGN, N2, and S2) of NGC 7319 (see Figs. 1, 2, and 4) shown at rest-wavelength (assuming $z = 0.02251$). The continuum level is determined from a linear fit to the flux at the edges of the covered spectral range in each channel. A point-source aperture correction is applied to the AGN spectra. From top to bottom, the panels show the spectra from MRS channel 1, 2, 3, and 4, respectively. Region S2 is not covered by the fields of view of channels 1 and 2. The wavelength of the emission lines are indicated in blue for rotational H_2 transitions, in orange for H recombination lines, and in green, red, and purple for transitions from low-ionization ($\text{IP} < 13.6$ eV), intermediate-ionization ($13.6 \text{ eV} < \text{IP} < 54.4$ eV), and high-ionization ($\text{IP} > 54.4$ eV) species, respectively. The continuum subtracted spectra have been scaled and shifted for visualization purposes. In this figure, we shifted the channel 3 medium sub-band wavelength by $0.04 \mu\text{m}$ to correct for a wavelength calibration artifact (see Appendix A.1).

^a The H_2 S(1) $17.03 \mu\text{m}$ transition is affected by a wavelength calibration artifact which alters the line profile of the AGN and N2 spectra but not the observed line flux (see Appendix A.1).

Appendix C: Ionized and warm molecular gas velocity field

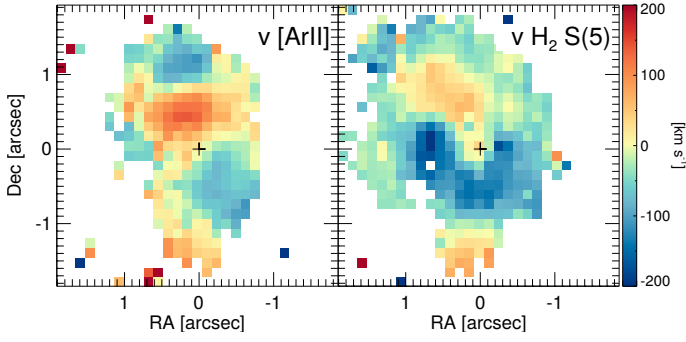


Fig. C.1: Velocity field, first moment, derived from the [Ar II] 6.99 μm (left) and H₂ S(5) 6.91 μm (right) emission lines. Same field of view as Figs. 2 and 3.

Appendix D: Mid-IR [Fe II] density diagnostics

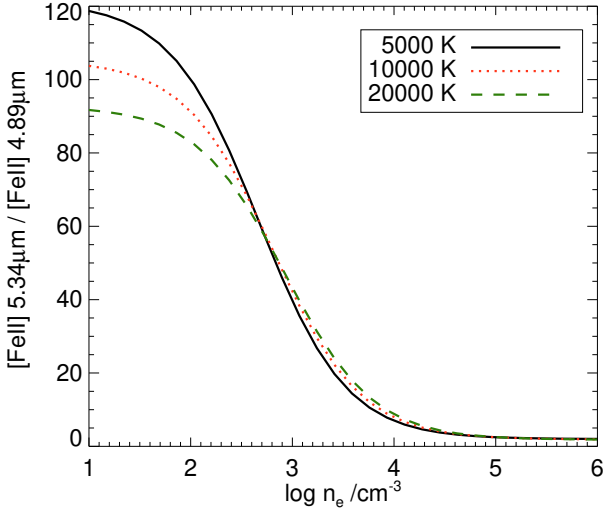


Fig. D.1: [Fe II] 5.34 μm /[Fe II] 4.89 μm ratio as function of the electron density at 5000 K (black solid line), 10000 K (red dotted line), and 20000 K (green dashed line). The [Fe II] 17.94 μm /[Fe II] 4.89 μm ratio is fixed an equal to 10.9 since both transitions have the same upper level ($3d^7 a_4 F_{7/2}$). Therefore, both transitions can be used interchangeably to determine the electron density together with the [Fe II] 5.34 μm line. The line emissivities are calculated using PyNeb (Luridiana et al. 2015) and the Fe⁺ atomic parameters from Smyth et al. (2019).